

RAD: A Dataset and Benchmark for Real-Life Anomaly Detection with Robotic Observations

Kaichen Zhou¹, [†]Yang Cao², [†]Taewhan Kim¹, Hao Zhao³,
Hao Dong¹, Kai Ming Ting⁴, Ye Zhu^{2*}

¹School of Computer Science, Peking University.

²School of Information Technology, Deakin University.

³Institute of AI Industry Research, Tsinghua University.

⁴School of Artificial Intelligence, Nanjing University.

*Corresponding author(s). E-mail(s): ye.zhu@ieee.org;

Contributing authors: kc.zhou2020@hotmail.com; charles.cao@ieee.org;

taewhank@stu.pku.edu.cn; zhaohao@air.tsinghua.edu.cn;

hao.dong@pku.edu.cn; tingkm@nju.edu.cn;

Abstract

Recent advancements in industrial anomaly detection have been hindered by the lack of realistic datasets that accurately represent real-world conditions. Existing algorithms are often developed and evaluated using idealized datasets, which deviate significantly from real-life scenarios characterized by environmental noise and data corruption such as fluctuating lighting conditions, variable object poses, and unstable camera positions. To address this gap, we introduce the Realistic Anomaly Detection (RAD) dataset, the first multi-view RGB-based anomaly detection dataset specifically collected using a real robot arm, providing unique and realistic data scenarios. RAD comprises 4287 images across 13 categories and 4 defect types, collected from more than 60 viewpoints, providing a comprehensive and realistic benchmark. This multi-viewpoint setup mirrors real-world conditions where anomalies may not be detectable from every perspective. Moreover, by sampling varying numbers of views, the baselines' performance can be comprehensively evaluated across different viewpoints. This approach enhances the thoroughness of performance assessment and helps improve the algorithm's robustness. Besides, we propose a preprocessed method to support 3D multi-view-based anomaly detection algorithms by improving pose estimation accuracy.

[†]: Yang Cao and Teawhan Kim are co-second authors who contributed equally to this work. Their order is determined by the alphabetical order of their last names.

We systematically evaluate state-of-the-art RGB-based models using RAD, identifying limitations and future research directions. The code and dataset could found <https://github.com/kaichen-z/PAD>. 1. proof-reading. 2. re-arrange code and dataset. 3. re-run experiments. (for new dataset) 4. make sure the final version.

Keywords: Anomaly Detection, Robotics, Pose Estimation

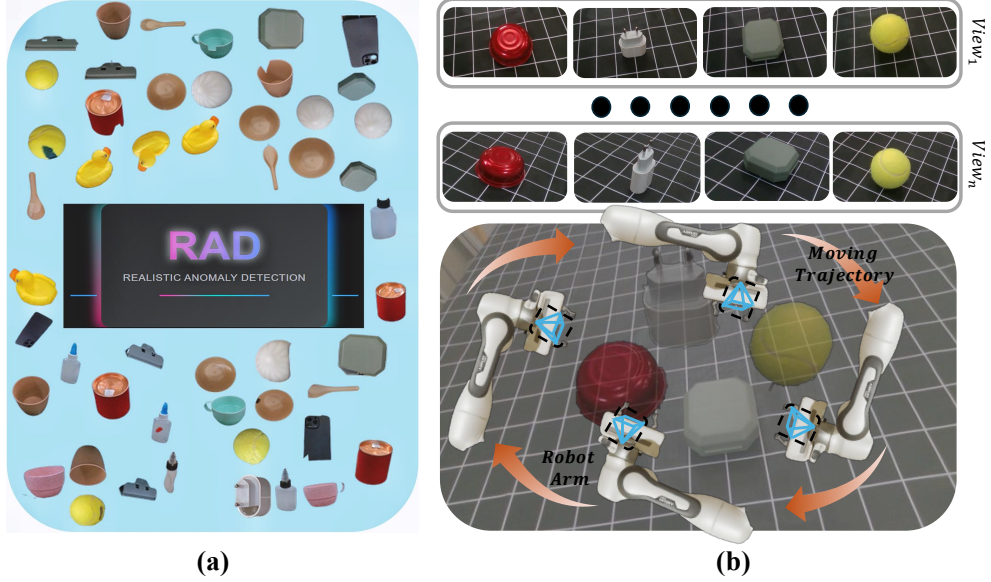


Fig. 1 Illustration of RAD Dataset. Figure (a) illustrates our daily objects family in RAD dataset. Figure (b) demonstrates the dataset collection process employing robot arms.

1 Introduction

The Need for a Real-Life Anomaly Detection Dataset with Robotic Observations: The rapid integration of robotics into modern industrial pipelines has revolutionized manufacturing processes, significantly enhancing efficiency and effectiveness. As the use of robots becomes more widespread, anomaly detection has emerged as a crucial component of these pipelines. However, the development and evaluation of most existing industrial anomaly detection algorithms rely on datasets collected under idealized conditions, where sensors provide perfect observations. Consequently, implementing reliable anomaly detection in real-world robotic systems presents several challenges. One major challenge stems from the presence of noise in robotic observations, which can be attributed to various external and internal factors [1–3]. External factors, such as fluctuating lighting conditions, varying object poses, and inconsistent backgrounds, can introduce significant noise into the data. Moreover, internal factors, including imperfect camera calibration, suboptimal movement control, and sensor inaccuracies, further complicate the detection process. These sources of noise may compromise the reliability and effectiveness of anomaly detection algorithms. To address these challenges and bridge the gap between research and real-world

applications, there is a pressing need for a benchmark dataset that accurately represents the complexities and variabilities of real-life industrial scenarios. Such a dataset should encompass diverse conditions and account for the various sources of noise that can affect robotic observations. By providing a realistic and comprehensive testbed, this dataset would enable the development and benchmarking of more robust and effective anomaly detection algorithms.

The availability of a representative benchmark dataset is crucial for advancing the field of industrial anomaly detection using robotics. It would allow researchers and practitioners to evaluate and compare the performance of different algorithms under realistic conditions, facilitating the identification of strengths and weaknesses. Furthermore, it would drive the development of novel approaches that can handle the challenges posed by real-world environments, ultimately leading to more reliable and efficient anomaly detection in industrial settings.

Limitation of Current Datasets: Existing RGB-based datasets such as LOCO-AD [4], MVTec AD [5, 6] and MPDD [7] primarily focus on single-view RGB observations of objects. This approach misses the critical 3D structural information of the real world, thereby limiting their applicability.

In response to the limitations inherent in 2D datasets, recent research has increasingly focused on the development of 3D anomaly detection datasets, but they also have their own constraints. For instance, MVTec 3D-AD [8] only provides single-view point clouds and suffers from low resolution, which affects the quality and accuracy of the anomaly detection. While Eyescandies [9] offers higher-quality data, it is limited to simulated environments and does not include real-world data. To address the shortcomings of MVTec 3D-AD and Eyescandies, Real3D-AD [10] offers point clouds of entire objects. However, obtaining a complete point cloud of an object in real-life conditions is challenging. In practical industrial scenarios, objects are not typically suspended in mid-air and are often placed randomly, complicating comprehensive point cloud data acquisition. Instead of directly providing point cloud information, PAD [11] offers multi-view RGB data, which can be considered a 3D representation akin to Neural Radiance Fields (NeRF) [12]. However, PAD mainly focuses on simulated data and includes only a small and simple real-world dataset. These limitations highlight the need for a more robust and comprehensive dataset that can accurately reflect the complexities and variabilities of real-world industrial environments. Furthermore, Real-IAD [13] introduced a large-scale, real-world, multi-view industrial anomaly detection dataset. However, this dataset provides only five views per object, while in real-world scenarios, objects can appear in a range of random poses, making five fixed observations insufficient to fully capture the variability encountered in practice.

Based on the analysis above, we introduce RAD, a multi-view RGB-based anomaly detection dataset designed to test the robustness and scalability of existing anomaly detection algorithms on real-world data. Our dataset includes 13 different objects and captures over 4287 images from multiple viewpoints (around 60s), providing a comprehensive testbed for evaluating algorithm performance. RAD records four distinct types of defects, encompassing both texture-based and geometry-based anomalies for each object. This configuration simulates real-life situations where defects may not

always be visible from the current viewpoint, and the number of views can vary across different scenarios. To evaluate the quality and versatility of our dataset, we conducted assessments using two distinct types of algorithms: 2D RGB-based and 3D multi-view RGB-based. While 2D RGB-based algorithms have demonstrated impressive performance in RGB-based anomaly detection tasks, their lack of consideration for 3D pose makes them less preferable compared to 3D multi-view RGB-based algorithms for multi-view anomaly detection datasets [11, 14]. However, given that our dataset was collected using real robots shown in Figure. 1, it intrinsically contains noise related to camera calibration and robot positioning. This noise is critical as it significantly affects the performance of the algorithms. Consequently, the direct application of conventional 3D-based algorithms frequently leads to underperformance. To enable effective use of 3D multi-view RGB-based algorithms, we propose a data pre-processing method that accurately estimates camera poses. Building on more accurate pose estimation, we highlight the potential to construct a 3D point cloud using multi-view RGB observations. Despite these efforts, both multi-view RGB-based and 3D point cloud-based algorithms encounter challenges due to variable lighting conditions and the high-specularity of certain objects. This highlights the need for more robust algorithms in future research.

The main contributions of this dataset are summarized as follow:

- We introduce the first real-life multi-view anomaly detection dataset with robotic observations, featuring 13 object categories and both texture-based and geometry-based defects. The dataset effectively captures the noisy environments experienced by real robots, bridging the gap between research and real-world applications.
- We propose the Noisy-Pose-Based Anomaly Detection (NAD) challenge to evaluate algorithm performance under noisy pose conditions and enhance robustness in real-robot scenarios. The NAD challenge provides a standardized benchmark for assessing the effectiveness of anomaly detection algorithms in handling real-world challenges.
- We propose advanced data preprocessing methods that address the challenges associated with noisy and inconsistent data. These tools facilitate the development and evaluation of novel algorithms that can leverage the rich information available in multi-view and point cloud data.
- We evaluate the performance of 2D RGB-based, 3D multi-view based, and 3D point cloud-based algorithms on our dataset, providing a detailed analysis of the results. This evaluation highlights the strengths and weaknesses of each approach and identifies areas for future improvement.

2 Related Work

2.1 Existing Datasets for 3D Anomaly Detection

Anomaly detection and localization is an important task in industrial quality control [17], and there is a wide range of datasets for 2D industrial anomaly detection, such as MVTec AD [5], MPDD [7] and VisA [15]. These datasets spawned many related

Table 1 Comparison of RAD and existing industrial anomaly detection datasets. RGB, D, PC, and NM stand for RGB image, Depth, Point Cloud, and Normal Maps, respectively. Surface represents the objects that are transparent or specular. “R.” refers to the dataset with a real-life environment. “S.” refers to the dataset with simulation environment.

Datasets	Representation	#Class	# Normal	#Abnormal	#Shoots
MVTec AD [5] (R.)	RGB	15	4,096	1,258	1
MPDD [7] (R.)	RGB	6	1,064	282	1
VisA [15] (R.)	RGB	12	9,621	1,200	1
MVTec 3D-AD [16] (R.)	RGB/D/PC	10	2,904	948	1
Eyecandies [9] (S.)	RGB/D/NM	10	13,250	2,250	1
Real3D-AD [10] (R.)	RGB/D/PC	12	652	602	360°
PAD [11] (S.)	RGB	20	4,960	4,412	Around 20
PAD [11] (R.)	RGB	10	271	490	Around 20
Real-IAD [13] (R.)	RGB	30	99,721	51,329	5
RAD (Ours) (R.)	RGB	13	1,224	3,063	68
Datasets	View	Color	Surface	Train. Pose	Test. Pose
MVTec AD [5] (R.)	Single	Diverse	Specular	2D	2D
MPDD [7] (R.)	Single	Diverse	Specular	2D	2D
VisA [15] (R.)	Single	Diverse	Specular	2D	2D
MVTec 3D-AD [16] (R.)	Single	Diverse	Specular	3D	2D
Eyecandies [9] (S.)	Single	Diverse	Transparency	3D	2D
Real3D-AD [10] (R.)	Multi	Diverse	Transparency	3D	2D
PAD [11] (S.)	Multi	Diverse	Specular	3D	2D
PAD [11] (R.)	Multi	Diverse	Specular	3D	2D
Real-IAD [13] (R.)	Multi	Diverse	Specular	3D	3D
RAD (Ours) (R.)	Multi	Diverse	Specular	3D	3D

works on 2D industrial anomaly detection [18–20], these methods are mainly categorised into image reconstruction [21–26] and feature embedding[27–32]. Additionally, the domain of few-shot learning [33, 34] explores enhancements in model performance under fixed data scenarios, whereas anomaly synthesis [35–37] investigates techniques for generating synthetic anomalies to augment training datasets, thereby improving model robustness. However, since RGB images do not contain spatial information and have a single-view, 2D anomaly detection makes it difficult to detect occlusions or geometric anomalies due to lighting or viewing angle.

Some 3D datasets have been proposed to extend anomaly detection from 2D to 3D, which have been compared in Table. 1. MVTec 3D-AD [16] dataset is the first comprehensive 3D dataset with 10 different object categories that is inspired by real-world visual inspection scenarios. However, the MVTec 3D-AD can only provide information from a single viewpoint and lacks RGB information from a full range of viewpoints. In addition, the MVTec 3D-AD dataset has a single background and ambient light, making it difficult to simulate realistic and complex industrial scenes. MPDD [7] dataset supplies multi-view information on metal parts and simulates 12 different types of defects, however, it is constrained in data scale. Eyecandies [9] dataset is a synthetic dataset consisting of synthetic candy views captured under a variety of different lighting conditions. However, it is also limited to single-view and there are differences between the synthetic and real-world data. Real 3D-AD [10] dataset is introduced to expand the object information to 3D space. Real 3D-AD uses a point cloud scanner to

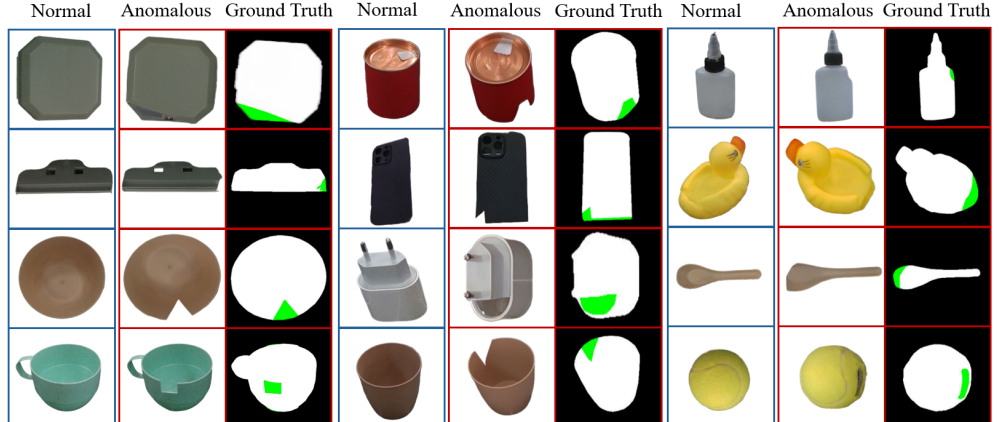


Fig. 2 Examples of missing anomaly and annotation for each object. The blue frame indicates the normal images in the training dataset. The red frame denotes the anomalous images and ground truth in the testing dataset. The green color is the annotation of the missing region. Each image is a randomly selected single view from each object in RAD.

scan the object with a full range view and provides the data directly in a point cloud format, thus both the training set and testing set of Real3D-AD contains multi-view information on objects but it only provides spatial information. PAD [11] contains 3D scans of 20 objects, which are used to explore the problem of pose-agnostic anomaly detection. Real-IAD [13] is another latest multi-view datasets that contains 30 objects, but it only provides the information from 5 shooting angles.

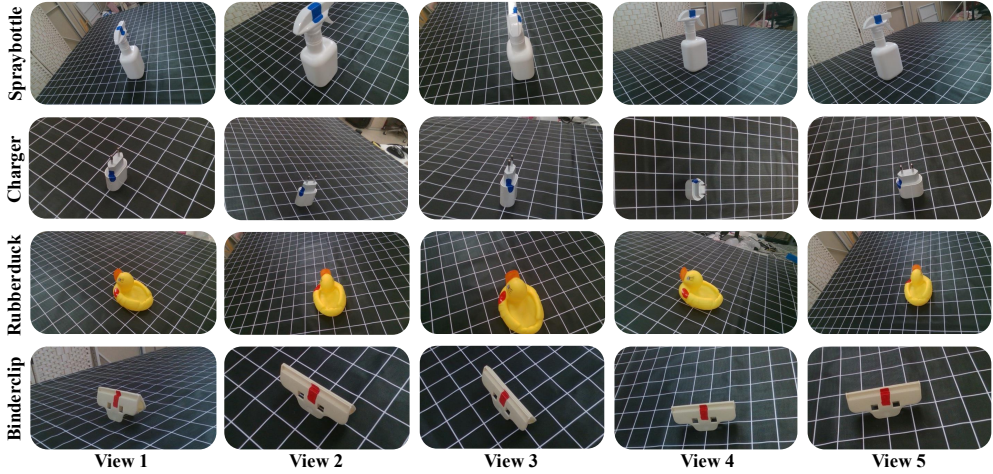


Fig. 3 Examples of multi-view information. This figure displays a subset of RAD data, illustrating that multiple view observations are provided for each object to support 3D-based anomaly detection algorithms.

2.2 Unsupervised 3D Anomaly Detection

Despite considerable advancements in 2D anomaly detection, the domain of 3D anomaly detection (3D-AD) continues to develop, and substantial challenges persist,

particularly in the effective integration of depth and RGB data while maintaining optimal performance. AST [38] combines RGB and depth information to detect defects but the depth information is only used to remove background, anomaly detection is still based on the 2D detection method. M3AD [39] fuses and aligns the feature extracted from the point cloud and RGB images to improve the anomaly detection performance. CPMF [40] combines local geometrical information in 3D modality and global semantic information in the generated pseudo-2D modality to obtain better detection results. Reg3D-AD [10] also employs a dual-feature representation approach, which jointly leverages local features and global representations to detect anomalies in the proposed Real 3D-AD dataset effectively. OmniposeAD [11] addresses pose-agnostic anomaly detection problem by using Neural Radiance Field (NeRF) [12] to reconstruct normal images and refine the pose with image retrieval techniques and iNeRF [41].

2.3 3D Reconstruction

The goal of 3D Reconstruction is to generate a 3D model that accurately captures the shape, geometry, and appearance of a real-world object. The existing 3D reconstruction methods can be categorized as following [42]: **Point cloud** is a set of 3D points used to represent the surface or structure of an object or scene [43–45]. On the one hand, sparse point cloud reconstruction methods [46, 47] aim to generate a relatively small number of 3D points that capture the essential structure and geometry of the scene or object. The focus is on identifying and reconstructing key features or landmarks rather than creating a detailed, continuous representation. On the other hand, dense point cloud reconstruction methods [48] aims to create a highly detailed and dense point cloud that captures the complete surface geometry of the object or scene. **Voxel**-based reconstruction methods represent the surface of a 3D object by using fixed-size cubes as the smallest unit, including 3D voxel grids [49–52] and octants [53, 54]. A voxel represents a discrete, cubic volume element within a regularly spaced 3D grid and an octree recursively subdivides the 3D space into eight equal-sized octants until a predefined maximum depth or resolution is achieved. Voxel grids are memory-intensive, especially for high-resolution reconstructions. **Mesh**-based methods define the surface geometry of an object via vertices, edges, and faces [55–60]. Meshes can provide a high-quality and accurate representation of the object’s surface, capturing fine details and sharp features, while Mesh-based reconstruction is sensitive to noise and incomplete data, and complex surfaces reconstruction may result in large and dense meshes. **Neural Radiance Fields** (NeRF) [12]-based reconstruction encodes a 3D scene as a continuous function that maps 3D coordinates and viewing directions to color and density values, leveraging a neural network trained on a set of 2D images captured from different viewpoints. This implicit learning allows the network to capture the 3D structure and appearance of the scene. NeRF has been used by PAD [11] to re-rendering high quality images for industrial anomaly detection. NeRF-based 3D surface reconstruction offers several advantages over traditional point cloud-based approaches. NeRF requires only a set of 2D images as input, eliminating the need for explicit 3D scanning or depth information. However, the computational complexity and the requirement for extensive training data and time pose challenges in achieving high-quality reconstruction results.

3 Description of RAD dataset

In this section, we delineate the data acquisition and ground-truth annotation processes for the proposed RAD. Utilizing category and defect information, we will furnish relevant dataset statistics.

3.1 Data Acquisition

Prototype construction

RAD data acquisition process leverages the interactive maneuverability and dynamic data capture capabilities of a robotic arm, facilitating data collection from various angles and perspectives. The robotic arm, equipped with a high-resolution RGB-D camera, captures detailed geometrical and textual data of each object from different angles. Specifically, the prototype construction utilizes a Franka Emika Panda robotic arm as in [61], which carries an "Intel RealSense Depth camera D415 Webcam 3D" as in [62] with a resolution of 1280×720 pixels, to capture high-resolution images from 68 predefined angles, completing a full 360° revolution. The object is centrally positioned within the robotic arm's operational range to ensure consistent imaging across all angles. Each angle's coordinates are precisely recorded to maintain uniformity in data capture. Nevertheless, owing to the mentioned noises in the introduction, we exclusively offer RGB data and 68 views for each category, shown in Figure. 2 and Figure. 3.

In contrast to other data acquisition methods such as using multiple fixed-position cameras or a static point cloud scanner setup, the robotic arm approach offers significant advantages in flexibility and efficiency. Benchmark datasets such as PAD [11] require multiple cameras to cover different angles for shooting, and point cloud scanners [10] need to rotate objects for all-round scanning, while robotic arms can achieve full coverage with a single camera without moving the object. This adaptability makes the robotic arm particularly suitable for industrial assembly lines, where space and setup time are critical considerations. Moreover, automating the data acquisition process with a robotic arm minimizes human error and optimizes the efficiency and reliability of data collection, enhancing the overall robustness of the collection system.

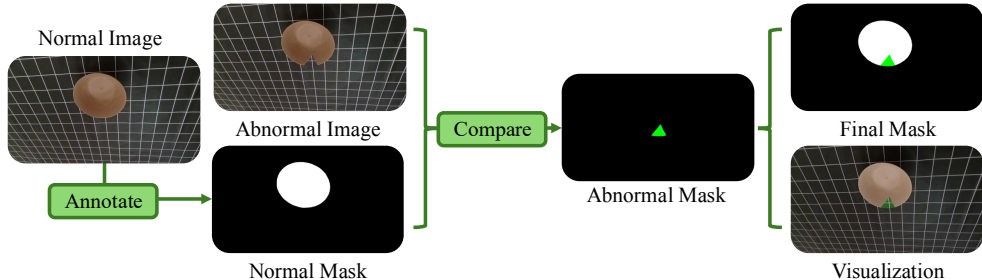


Fig. 4 Illustration of Annotation Procedure: This diagram illustrates the annotation process for identifying missing components. Annotations for missing parts primarily rely on comparing defective objects with normal ones.

Details of data annotation

Our pipeline comprises two main parts for annotating defects. First, we annotate the object regions in the normal image. Then, we compare this annotation with the abnormal image. By combining these annotations, we generate a final defect mask. This final mask is overlaid onto the abnormal image to produce the visualization shown in the right part of the Fig. 4. This process allows us to visually highlight and identify defects effectively within the images.

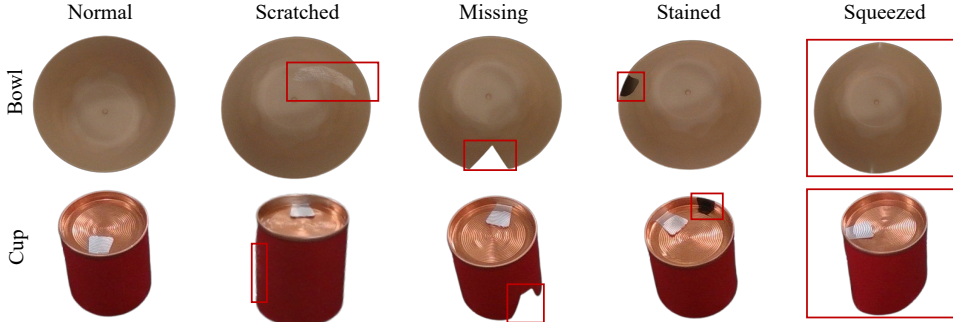


Fig. 5 Examples of four defect types. The red frames denote the anomaly regions. Note: entire objects with squeezed anomalies are marked as anomaly regions due to the overall deformation.

Anomaly types

To ensure the dataset's utility in evaluating robustness against common industrial defects, we simulated four prevalent classes of anomalies as follows:

- **Scratched** is generated by scribing the object's surface with a sharp implement.
- **Missing** is simulated by removing segments from the objects.
- **Stained** is generated by applying discoloring agents to localized areas of the objects.
- **Squeezed** is created by applying pressure to deform parts of the objects.

Figure. 5 demonstrates the example of four different defects of cup and bowl. It is important to note that, due to the varying materials of the items, simulating squeezed anomalies for robust objects presents significant challenges. Consequently, binderclip, box, charger, and phonecase do not include the squeezed defect type.

Labor and time-consumption

The use of a robotic arm for data acquisition represents a significant enhancement in the efficiency and scalability of industrial anomaly detection. By pre-configuring shooting angles within the robotic arm's control system, we minimize human intervention primarily to the task of replacing objects for capture. This automation not only expedites the data collection process but also ensures consistency and repeatability across diverse datasets, facilitating more extensive and robust data collection endeavors.

Nevertheless, despite the streamlined data acquisition facilitated by the robotic arm, the subsequent phase of data annotation poses substantial challenges in terms of

Table 2 Dataset statistics. The "Type" category represents the count of distinct object types. "Single" under "Attribute" indicates objects typically have one color. "Multi." under "Attribute" indicates objects typically have multiple colors. "Spec." under "Attribute" indicates objects with specular surfaces. "Miss." indicates objects with missing defects. "St." indicates objects with stained defects. "Sc." indicates objects with scratched defects. "Sq." indicates objects with squeezed defects.

Category	Type	Attribute	Miss.	St.	Sc.	Sq.	Normal	Total
Binderclip	2	Single	136	136	136	0	136	544
Bowl	1	Single	68	68	60	68	68	332
Box	1	Single	45	68	68	0	68	249
Can	1	Multi./Spec.	41	68	4	68	68	249
Rubberduck	1	Multi.	58	60	68	68	68	322
Spraybottle	1	Single/Spec.	52	62	68	68	68	318
Cup1	1	Single	68	66	61	68	68	331
Gluebottle	2	Multi./Spec.	51	23	24	68	136	302
Charger	1	Multi./Spec.	66	66	5	0	68	205
Cup2	3	Single	68	29	66	68	204	435
Phonecase	2	Single	68	68	68	68	136	408
Spoon	1	Single	68	66	51	68	68	321
Tennisball	1	Multi.	67	68	68	0	68	271

time and resource allocation. In our methodology, the images captured from each configured angle by the robotic arm were annotated using Adobe Photoshop, a process requiring precise manual intervention to identify and label all anomalous pixels. This meticulous process of annotating images from multiple perspectives ensures a comprehensive representation of potential anomalies but took approximately one months to complete for the dataset.

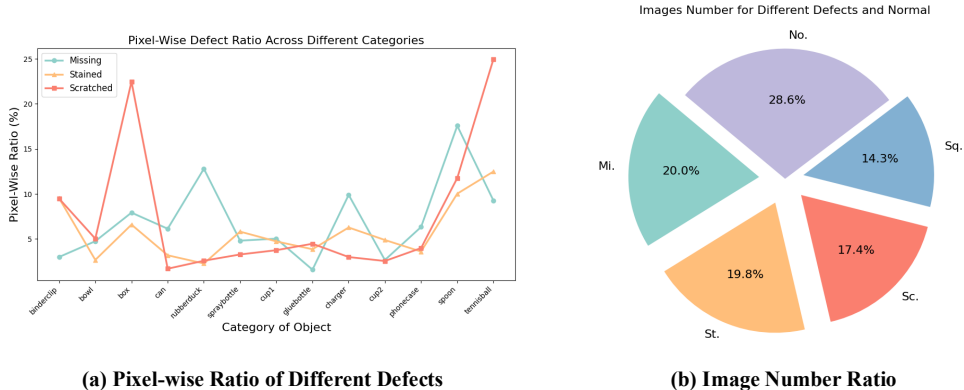


Fig. 6 Dataset Metrics. (a) illustrates the pixel-wise ratio within each defect across various categories. (b) shows the total number ratio of each defect in RAD. "Mi." refers to Missing. "No." refers to Normal. "Sq." refers to Squeezed. "Sc." refers to scratched. "St." refers to "Stained".

3.2 Dataset Statistics

The statistical details of the RAD dataset are outlined in Table. 2 and Figure. 6, which enumerates the dataset categories, the number of training prototypes, and the counts of both normal and various abnormal samples within the test dataset. The RAD dataset comprises a total of 5,848 samples, distributed across 12 distinct objects that encompass multiple domains, including kitchenware, toys, and daily necessities. The categories in RAD dataset exhibit significant diversity in shapes and appearances, providing extensive semantic and geometrical exploration spaces that facilitate a wide range of research objectives. In addition, the data set also includes metadata (camera pose) for each image, which is essential for nuanced analyses and model training enhancements.

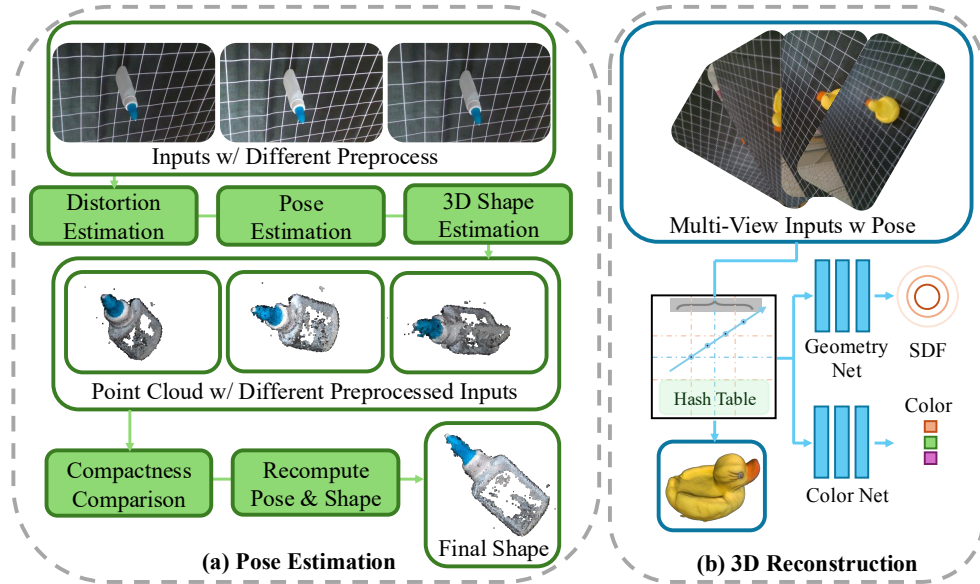


Fig. 7 Pipeline of Data Preprocessing. The data preprocessing involves two steps: the first step is pose estimation, followed by 3D reconstruction in the second step.

4 Methodology

Considering the challenges of the NAD problem, directly applying 3D-based anomaly detection methods introduces significant uncertainty. Current multi-view methods, such as MVSNeRF [63], NEUS [64], and 3D Gaussian [65], depend heavily on accurate pose estimation. These multi-view reconstruction methods specifically rely on high-quality pixel-wise matching between different images, which is significantly influenced by the relative positional information between frames. To address this issue, we propose a pipeline to estimate the pose from different views, enabling multi-view based anomaly detection algorithms. Furthermore, we apply 3D reconstruction to create a 3D point cloud, facilitating the use of 3D point cloud-based anomaly detection algorithms. Our

pipeline is demonstrated in Figure 7. It is important to note that our paper primarily focuses on providing an anomaly detection dataset. Our methodology aims to offer a potential solution for future research.

Self-Supervised Pose Estimation: Directly using the poses recorded by the robot may introduce noise and errors due to camera calibration and robot control inaccuracies. To address this issue, we implement the following pose estimation pipeline: Distortion Estimation: Given a series of images $\{I \in \mathbb{R}^{H \times W \times 3}\}$ and corresponding masks $M \in \mathbb{R}^{H \times W}$, we first estimate the distortion parameters based on a radial camera model. Pose Estimation: Using the obtained radial parameters, we perform exhaustive feature matching between image pairs, which helps to the pose estimation. This process helps in reconstructing a sparse point cloud as detailed in [66–69]. 3D Shape Estimation: With the help of estimated feature and pose information, the sparse point cloud could be estimated. While the sparse point cloud alone is insufficient for evaluating pose estimation quality. Therefore, we apply the patchwise method proposed in [70] to reconstruct a relevant dense point cloud.

By analyzing the reconstructed relevant dense point clouds, we found that directly implementing this pipeline does not always yield reasonable pose estimations when the ground truth pose information is missing. To generate more reasonable pose information in a self-supervised setting, we propose modifying the previous pipeline by adding a preprocessing step and a compactness comparison step. Preprocess: Specifically, we separately apply the following three preprocessing algorithms: brightness adjustment, contrast adjustment, and gamma adjustment. Among them, brightness adjustment can be expressed as:

$$I_{\text{adjust}}^{\text{br}}(x, y) = \min(\max(I(x, y) + \Delta B, 0), 255), \quad (1)$$

where ΔB is a constant value.

Contrast adjustment could be written as:

$$I_{\text{adjust}}^{\text{con}}(x, y) = \min(\max(I(x, y) - M \cdot C + M, 0), 255), \quad (2)$$

where M is the midpoint or mean intensity of the image. For an 8-bit grayscale image, $M = 128$, or you can use the mean intensity of all pixel values as M . C is the contrast factor.

Gamma adjustment could be written as:

$$I_{\text{adjust}}^{\text{ga}}(x, y) = \min\left(\max\left(255 \cdot \left(\frac{I(x, y)}{255}\right)^\gamma, 0\right), 255\right), \quad (3)$$

where γ is the gamma value that controls the adjustment. The pixel intensities are first normalized by dividing by 255 (for 8-bit images) to map values to the range $[0, 1]$, then raised to the power of γ , and finally scaled back to the range $[0, 255]$. Compactness Comparison: By applying different preprocessing algorithms, we obtain different sets of images, including $\{I\}$ and $\{I_{\text{adjust}}^i\}$, where I_{adjust}^i indicates images with various adjustment algorithms. Based on these different sets, we can generate distinct sets of pose information. Consequently, different point clouds are estimated. Since we

cannot evaluate the pose estimation results directly, we estimate the compactness of the point clouds using the following:

$$\text{Compactness} = \frac{\text{Volume}}{(\text{Surface Area})^2}, \quad (4)$$

where Volume is the volume of the convex hull of the point cloud. Surface Area is the surface area of the convex hull.

This compactness value allows us to assess the pose estimation quality to some extent. We then select the pose estimation that produces the best compactness value (lowest) and apply it to images within that category. This pipeline helps ensure more accurate pose estimation and improves the overall quality of the 3D reconstruction process. This pipeline is shown in Figure 7 (a). Generated 3D shapes for the category "Binderclip" is shown in Figure. 8.

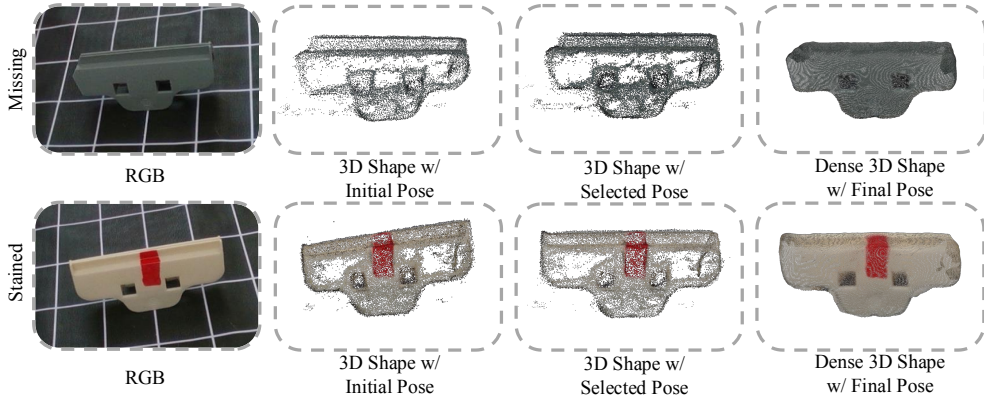


Fig. 8 Visualization of Data Preprocessing Results. The first image represents the original figure, followed by the point cloud generated from initial pose estimation. The third image depicts the point cloud reconstruction through refined pose estimation, while the final image showcases the dense point cloud estimation.

3D point cloud Reconstruction: Based on the estimated pose information for each image, we perform multi-view mesh reconstruction, which can then be used for subsequent 3D point cloud-based anomaly detection methods. We follow the pipeline established by Neuralangelo [64] to reconstruct the 3D mesh. This is realized by a network that takes a feature considering the 3D point position as input and predicts the surface information. The surface is represented by the zero-level set of the Signed Distance Function (SDF): $S = \{p \in \mathbb{R}^3 | \text{sdf}_\theta(p) = 0\}$. Following Neuralangelo [64], we compute opaque density function $\rho(t)$ from S . To make the depth supervision differential, we could derive the rendered depth as in [71]:

$$\hat{D} = \sum_{j=1}^{N_S} T_j \alpha_j t_j, \quad T_j = \prod_{k=1}^{j-1} (1 - \alpha_k), \quad \alpha_j = 1 - \exp(- \int_{t_j}^{t_{j+1}} \rho(t) dt) \quad (5)$$

where t is the z value from the sampled point to the camera origin and N_S is number of sampled points along each ray. Following [72, 73], give a point p_t on the ray of

a target frame, a network takes the position and view direction as input to predict the color information. Based on the volume rendering in NeRF [12], the final color is computed as: $\hat{C} = \sum_{j=1}^{N_S} T_j \alpha_j c_j$, where c_j is the predicted radiance and N_V is the number of source views. This structure is shown in Figure 7 (b).

Discussion: Why it is RGB-Based? The primary reason we do not provide depth images is that the LIDAR sensor cannot accurately predict point positions when the object is close to the camera. However, to capture detailed information about the objects, it is necessary to position the camera near them. This is especially crucial in our scenario, where most of the objects are small. **Why this dataset is essential?** Despite the advancements made with current anomaly detection datasets, most of them focus on simulation environments or real-life datasets with ideal conditions, which differ significantly from noisy real-world settings. To bridge this gap, we propose a dataset that accounts for multiple types of noise, including diverse object positions, varying lighting conditions, noisy robot movements, and imperfect camera calibration. We also offer a potential pipeline to address these challenges. However, despite our efforts, this dataset still presents unresolved challenges.

5 Experiments

Problem Definition: For each object, we provide N images for the normal case and M images for cases with defects. The model is trained using the N images or the 3D information estimated from these images, such as point clouds. During testing, the model is used to determine whether an image from the M images contains defects and to generate a mask identifying the defects. In the RAD case, we consider four different types of defects, including both texture-based and geometry-based defects.

Challenge: (a) The training and testing images are not aligned, in terms of object pose. (b) The training and testing images are subjected to different lighting conditions. (c) The 3D poses of the training and testing images are not accurate due to camera calibration noise.

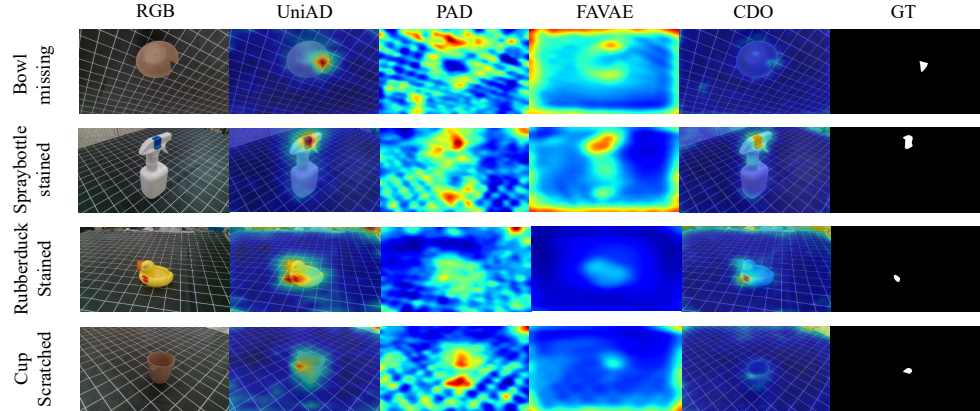


Fig. 9 Visualization of Pixel-Wise Anomaly Detection Baselines. The heatmap visualization illustrates the ground truth and inference results for two anomalous objects, Bowl and Spraybottle.

Table 3 Quantitative comparison. This table shows the performance of various models on the RAD dataset with masking the background. The dataset is evaluated in terms of Pixelwise-ROCAUC and Imagewise-ROCAUC. P-ROC refers to Pixelwise-ROCAUC. I-ROC refers to Imagewise-ROCAUC.

Model	Metric	binder.	bowl.	box	can	charger	cup1.	cup2.
FastFlow [74]	P-ROC	94.83%	71.70%	96.60%	90.40%	95.60%	74.10%	92.45%
	I-ROC	69.60%	67.00%	60.30%	49.60%	37.30%	47.50%	76.65%
STPM [75]	P-ROC	94.80%	91.90%	94.30%	95.30%	95.40%	93.80%	94.48%
	I-ROC	69.97%	75.90%	79.50%	68.90%	63.50%	65.50%	69.68%
CFA [76]	P-ROC	99.35%	90.88%	98.99%	97.71%	99.57%	94.61%	95.12%
	I-ROC	90.58%	82.53%	86.74%	92.70%	89.54%	80.52%	73.09%
cflow [32]	P-ROC	99.66%	96.68%	99.66%	99.02%	99.85%	97.97%	97.96%
	I-ROC	88.18%	94.66%	94.17%	95.52%	85.56%	84.45%	77.49%
Gau	P-ROC	99.00%	96.00%	98.20%	98.80%	99.30%	97.30%	96.53%
	I-ROC	21.20%	22.20%	11.80%	27.50%	8.00%	21.20%	19.35%
UniAD [24]	P-ROC	99.21%	95.70%	99.32%	98.90%	99.64%	97.56%	97.29%
	I-ROC	65.74%	63.89%	67.71%	67.28%	51.74%	57.67%	65.10%
FAVAE [77]	P-ROC	99.17%	95.70%	98.20%	99.20%	98.90%	98.30%	97.23%
	I-ROC	57.67%	58.90%	51.90%	55.90%	54.00%	41.30%	54.55%
CDO [78]	P-ROC	99.55%	95.66%	99.50%	98.47%	99.70%	97.43%	97.85%
	I-ROC	80.34%	87.42%	91.10%	86.56%	84.75%	77.99%	79.07%
Model	Metric	glue.	phone.	rubber.	spoon.	spray.	tennis.	Aver.
FastFlow [74]	P-ROC	94.20%	96.83%	92.50%	97.00%	93.90%	99.20%	91.49%
	I-ROC	73.85%	91.13%	44.40%	79.50%	80.70%	99.90%	67.49%
STPM [75]	P-ROC	93.70%	93.40%	92.20%	90.20%	91.80%	94.50%	93.52%
	I-ROC	70.15%	79.03%	78.90%	84.70%	74.90%	96.80%	75.19%
CFA [76]	P-ROC	98.72%	97.29%	95.42%	99.00%	95.18%	99.28%	97.01%
	I-ROC	83.21%	81.86%	85.48%	86.83%	88.47%	99.23%	86.21%
cflow [32]	P-ROC	99.39%	98.92%	97.89%	99.69%	97.83%	99.66%	98.78%
	I-ROC	75.87%	99.10%	91.34%	95.83%	83.66%	100.00%	89.68%
Gau	P-ROC	98.95%	97.33%	96.70%	99.30%	94.20%	98.80%	97.72%
	I-ROC	20.80%	21.20%	21.50%	30.00%	20.50%	15.70%	20.07%
UniAD [24]	P-ROC	98.87%	98.54%	97.85%	99.31%	97.87%	99.49%	98.43%
	I-ROC	56.99%	67.24%	64.22%	81.07%	58.83%	66.16%	64.13%
FAVAE [77]	P-ROC	99.10%	97.35%	97.80%	99.50%	97.00%	99.00%	98.19%
	I-ROC	57.35%	42.05%	56.50%	73.20%	59.40%	54.60%	55.18%
CDO [78]	P-ROC	99.11%	98.62%	97.75%	99.23%	96.65%	99.62%	98.40%
	I-ROC	75.52%	92.81%	86.26%	89.24%	65.60%	99.23%	84.30%

5.1 Image-Based Baselines

We introduce a dataset comprising multi-view images and evaluate its fidelity using 2D feature embedding-based anomaly detection methodologies, specifically FastFlow [74], STPM [75], CFA [76], cflow [32] and CDO [78]. 2D reconstruction-based anomaly detection methodologies, specifically FAVAE [77] and UniAD [24]. These methods leverage neural networks to learn representations conducive to accurately reconstructing normal samples, with anomalies detected based on deviations in the reconstruction quality. Our findings are summarized in Table. 3 and Table. 4. Additionally, we investigate the effectiveness of PAD [11] and Splat [14], a 3D multi-view reconstruction-based algorithm. Notably, both 2D and 3D reconstruction-based methods exhibit limitations. The discrepancy is primarily attributed to misalignment between the training

Table 4 Quantitative comparison. This table shows the performance of various models on the RAD dataset **without masking** the background. The dataset is evaluated in terms of Pixelwise-ROCAUC and Imagewise-ROCAUC. P-ROC refers to Pixelwise-ROCAUC. I-ROC refers to Imagewise-ROCAUC.

Model	Metric	binder.	bowl.	box	can	charger	cup1.	cup2.
FastFlow [74]	P-ROC	93.73%	68.80%	96.70%	93.30%	94.70%	74.40%	76.10%
	I-ROC	51.17%	60.10%	60.50%	48.30%	40.50%	40.70%	61.80%
STPM [75]	P-ROC	82.73%	75.90%	83.90%	82.60%	85.80%	79.50%	79.58%
	I-ROC	59.90%	53.70%	62.70%	55.10%	49.10%	50.80%	61.28%
CFA [76]	P-ROC	98.00%	59.12%	97.84%	94.53%	98.64%	72.70%	74.37%
	I-ROC	61.49%	58.50%	70.47%	72.99%	61.40%	60.08%	64.06%
cflow [32]	P-ROC	98.83%	85.99%	98.63%	96.94%	99.51%	90.94%	90.18%
	I-ROC	68.14%	66.54%	75.75%	77.29%	80.37%	72.24%	65.32%
Gau	P-ROC	85.37%	64.10%	86.30%	89.30%	87.40%	74.80%	74.15%
	I-ROC	2.27%	2.70%	1.80%	4.70%	2.60%	2.30%	2.50%
UniAD [24]	P-ROC	96.93%	91.04%	96.87%	98.79%	98.04%	96.54%	93.43%
	I-ROC	53.59%	52.19%	52.87%	51.93%	53.28%	55.26%	54.13%
FAVAE [77]	P-ROC	67.90%	39.90%	58.30%	91.10%	83.70%	64.90%	59.65%
	I-ROC	66.20%	20.10%	51.30%	39.50%	35.30%	34.60%	24.78%
CDO [78]	P-ROC	96.65%	69.78%	96.55%	90.52%	97.01%	80.77%	82.12%
	I-ROC	60.51%	48.61%	59.85%	41.56%	55.31%	49.68%	64.93%
PAD [11]	P-ROC	90.50 %	75.80 %	90.30 %	98.10 %	97.30 %	96.10 %	79.20 %
	I-ROC	48.00 %	37.00 %	62.00 %	46.30 %	51.50 %	48.50 %	54.40 %
Splat [14]	P-ROC	98.30 %	96.80 %	97.90 %	98.20 %	99.70 %	98.00 %	97.45 %
	I-ROC	52.07 %	80.60 %	55.50 %	37.70 %	57.40 %	81.20 %	48.10 %
Model	Metric	glue.	phone.	rubber.	spoon.	spray.	tennis.	Aver.
FastFlow [74]	P-ROC	91.55%	97.00%	94.10%	96.70%	94.90%	98.20%	90.01%
	I-ROC	36.20%	65.48%	49.20%	78.40%	57.30%	78.50%	56.01%
STPM [75]	P-ROC	85.80%	85.88%	84.80%	79.10%	82.60%	85.40%	82.58%
	I-ROC	56.05%	73.23%	50.80%	59.70%	60.10%	71.50%	58.77%
CFA [76]	P-ROC	95.83%	95.67%	92.93%	98.43%	92.89%	98.76%	89.98%
	I-ROC	56.50%	73.77%	62.91%	73.96%	59.31%	83.53%	66.07%
cflow [32]	P-ROC	97.06%	94.02%	95.14%	98.55%	91.55%	98.50%	95.06%
	I-ROC	66.43%	66.09%	57.61%	82.17%	60.37%	79.37%	70.59%
Gau	P-ROC	78.40%	86.60%	85.70%	96.60%	90.50%	93.70%	84.07%
	I-ROC	1.60%	4.65%	5.60%	14.70%	20.60%	4.00%	5.39%
UniAD [24]	P-ROC	97.15%	96.16%	96.43%	97.69%	91.37%	98.86%	96.10%
	I-ROC	50.45%	51.72%	55.16%	50.02%	50.13%	51.29%	52.46%
FAVAE [77]	P-ROC	74.50%	59.58%	88.00%	85.70%	70.40%	92.00%	71.97%
	I-ROC	46.10%	32.28%	33.20%	53.10%	44.80%	49.30%	40.81%
CDO [78]	P-ROC	94.29%	93.36%	92.35%	96.16%	88.36%	97.26%	90.40%
	I-ROC	58.98%	53.60%	52.97%	53.45%	53.98%	66.34%	55.37%
PAD [11]	P-ROC	95.00 %	76.60 %	90.70 %	94.60 %	74.40 %	98.40 %	89.00%
	I-ROC	62.60 %	53.40 %	33.00 %	37.30 %	51.60 %	37.60 %	47.94%
Splat [14]	P-ROC	99.05 %	97.48 %	96.80 %	99.20 %	92.40 %	98.80 %	97.70 %
	I-ROC	42.25%	32.65 %	26.90 %	70.90 %	60.20 %	91.60 %	56.70 %

and testing sets, compounded by variations in lighting conditions that impact image quality. Our visualization is also consistent with our findings shown in Figure 9.

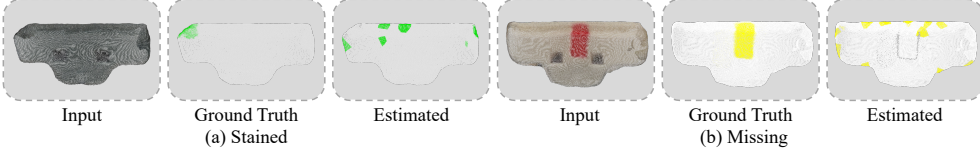


Fig. 10 Visualization of Point-Wise Anomaly Detection Baselines. The heatmap visualization illustrates the ground truth and inference results for two anomalous objects, Bowl and Spraybottle.

5.2 Point Cloud-Based Baselines

Additionally, we offer reconstructed point clouds derived from the multi-view RGB inputs. Our experimentation extends to include results obtained through the utilization of the 3D point-cloud-based algorithm BFT [79] shown in Figure. 10. Notably, it is imperative to acknowledge the inherent instability of current multi-view-based surface reconstruction algorithms. These algorithms are sensitive to variations in both lighting conditions and pose estimation, leading to inconsistent point cloud reconstructions across different categories. This inconsistency directly leads to the failure of the 3D point cloud-based anomaly detection algorithm BFT on our dataset. However, the generated point clouds also demonstrate the potential for applying 3D point cloud-based anomaly detection algorithms in multi-view anomaly scenarios, once the pose estimation and 3D shape reconstruction algorithms are properly implemented.

Table 5 Statistics for the RAD Subset. This subset is designed to evaluate the anomaly detection performance of different models across various defect types. For each object in the subset, an equal number of RGB frames is provided for all four defect categories.

Category/Defect	Missing	Stained	Scratched	Squeezed	Normal	Total
bowl.upright	49	49	49	49	220	367
cup1.upright	56	56	56	56	176	344
rubberduck	33	33	33	33	272	371
spraybottle	42	42	42	42	168	328

5.3 Ablation Study

In the previous section, we tested the anomaly detection performance of various algorithms across different categories of our dataset. Considering that our dataset also contains objects with various defect types, it is valuable to assess the model’s performance across these defects. Due to the differing materials and shapes of the objects, the number of defect images varies between objects. To address this, we extracted a subset from the original dataset to create a balanced set, ensuring an equal number of frames for each defect type. The statistics for this “new” dataset are provided in Table. 5. Given time and computational limitations, we applied two baselines to this balanced dataset. The quantitative results, shown in Table. 6, indicate that “scratched” and “squeezed” defects pose greater challenges for the baselines compared to “missing” and “stained” defects.

Table 6 Quantitative comparison. This table shows the performance of various models on the subset of RAD dataset, evaluated in terms of Pixelwise-ROCAUC and Imagewise-ROCAUC.

Model	Model	Defect	bowl	cup1	rubber.	spray.
FastFlow [74]	Pixel ROCAUC	Missing	85.00%	89.00%	91.00%	83.00%
	Image ROCAUC	Missing	87.00%	88.00%	97.00%	94.00%
	Pixel Recall	Missing	58.00%	83.00%	81.00%	82.00%
FastFlow [74]	Pixel ROCAUC	Scratched	55.00%	62.00%	65.00%	57.00%
	Image ROCAUC	Scratched	62.00%	54.00%	89.00%	77.00%
	Pixel Recall	Scratched	54.00%	52.00%	64.00%	55.00%
FastFlow [74]	Pixel ROCAUC	Stained	77.00%	80.00%	82.00%	81.00%
	Image ROCAUC	Stained	96.00%	83.00%	93.00%	91.00%
	Pixel Recall	Stained	77.00%	78.00%	77.00%	93.00%
FastFlow [74]	Pixel ROCAUC	Squeezed	59.00%	55.00%	56.00%	65.00%
	Image ROCAUC	Squeezed	70.00%	63.00%	89.00%	77.00%
	Pixel Recall	Squeezed	61.00%	53.00%	54.00%	65.00%
STPM [75]	Pixel ROCAUC	Missing	86.00%	87.00%	87.00%	87.00%
	Image ROCAUC	Missing	88.00%	89.00%	86.00%	97.00%
	Pixel Recall	Missing	84.00%	87.00%	88.00%	85.00%
STPM [75]	Pixel ROCAUC	Scratched	80.00%	81.00%	80.00%	81.00%
	Image ROCAUC	Scratched	83.00%	80.00%	86.00%	91.00%
	Pixel Recall	Scratched	80.00%	83.00%	80.00%	84.00%
STPM [75]	Pixel ROCAUC	Stained	61.00%	63.00%	59.00%	63.00%
	Image ROCAUC	Stained	66.00%	65.00%	60.00%	65.00%
	Pixel Recall	Stained	61.00%	64.00%	59.00%	62.00%
STPM [75]	Pixel ROCAUC	Squeezed	64.00%	65.00%	66.00%	68.00%
	Image ROCAUC	Squeezed	62.00%	66.00%	68.00%	74.00%
	Pixel Recall	Squeezed	67.00%	68.00%	67.00%	66.00%

6 Discussion

Conclusion: In this study, we introduce a novel anomaly detection dataset specifically designed to evaluate the robustness of existing anomaly detection algorithms when applied to real-world datasets captured by robots in the presence of environmental noise. Our dataset is characterized by multiple viewpoints and various defects for each object. Based on this dataset, we present a comprehensive preprocessing methodology aimed at facilitating the effective utilization of both 2D and 3D-based anomaly detection algorithms. Additionally, we assess the performance of different algorithms across various categories and defects within our dataset. **Limitation:** The categories offered within our dataset remain constrained, and the background against which data collection occurred is relatively uncomplicated. Moving forward, our future research endeavors will focus on expanding the range of categories provided.

References

- [1] Jakobi, N., Husbands, P., Harvey, I.: Noise and the reality gap: The use of simulation in evolutionary robotics. In: Advances in Artificial Life: Third European Conference on Artificial Life Granada, Spain, June 4–6, 1995 Proceedings 3, pp. 704–720 (1995). Springer
- [2] Parker, L.E.: Cooperative robotics for multi-target observation. *Intelligent Automation & Soft Computing* **5**(1), 5–19 (1999)
- [3] Lauri, M., Hsu, D., Pajarinen, J.: Partially observable markov decision processes in robotics: A survey. *IEEE Transactions on Robotics* **39**(1), 21–40 (2022)
- [4] Bergmann, P., Batzner, K., Fauser, M., Sattlegger, D., Steger, C.: Beyond dents and scratches: Logical constraints in unsupervised anomaly detection and localization. *International Journal of Computer Vision* **130**(4), 947–969 (2022)
- [5] Bergmann, P., Fauser, M., Sattlegger, D., Steger, C.: Mvtec ad—a comprehensive real-world dataset for unsupervised anomaly detection. In: Proceedings of the IEEE/CVF Conference on Computer Vision and Pattern Recognition, pp. 9592–9600 (2019)
- [6] Bergmann, P., Batzner, K., Fauser, M., Sattlegger, D., Steger, C.: The mvtec anomaly detection dataset: a comprehensive real-world dataset for unsupervised anomaly detection. *International Journal of Computer Vision* **129**(4), 1038–1059 (2021)
- [7] Jezek, S., Jonak, M., Burget, R., Dvorak, P., Skotak, M.: Deep learning-based defect detection of metal parts: evaluating current methods in complex conditions. In: 2021 13th International Congress on Ultra Modern Telecommunications and Control Systems and Workshops (ICUMT), pp. 66–71 (2021). IEEE
- [8] Bergmann, P., Jin, X., Sattlegger, D., Steger, C.: The mvtec 3d-ad dataset for unsupervised 3d anomaly detection and localization. arXiv preprint arXiv:2112.09045 (2021)
- [9] Bonfiglioli, L., Toschi, M., Silvestri, D., Fioraio, N., De Gregorio, D.: The eyecandies dataset for unsupervised multimodal anomaly detection and localization. In: Proceedings of the Asian Conference on Computer Vision, pp. 3586–3602 (2022)
- [10] Liu, J., Xie, G., Chen, R., Li, X., Wang, J., Liu, Y., Wang, C., Zheng, F.: Real3d-ad: A dataset of point cloud anomaly detection. *Advances in Neural Information Processing Systems* **36** (2024)
- [11] Zhou, Q., Li, W., Jiang, L., Wang, G., Zhou, G., Zhang, S., Zhao, H.: Pad: A dataset and benchmark for pose-agnostic anomaly detection. *Advances in Neural Information Processing Systems* **36** (2024)

- [12] Mildenhall, B., Srinivasan, P.P., Tancik, M., Barron, J.T., Ramamoorthi, R., Ng, R.: Nerf: Representing scenes as neural radiance fields for view synthesis. *Communications of the ACM* **65**(1), 99–106 (2021)
- [13] Wang, C., Zhu, W., Gao, B.-B., Gan, Z., Zhang, J., Gu, Z., Qian, S., Chen, M., Ma, L.: Real-iad: A real-world multi-view dataset for benchmarking versatile industrial anomaly detection. In: Proceedings of the IEEE/CVF Conference on Computer Vision and Pattern Recognition, pp. 22883–22892 (2024)
- [14] Kruse, M., Rudolph, M., Woiwode, D., Rosenhahn, B.: Splatpose & detect: Pose-agnostic 3d anomaly detection. In: Proceedings of the IEEE/CVF Conference on Computer Vision and Pattern Recognition, pp. 3950–3960 (2024)
- [15] Zou, Y., Jeong, J., Pemula, L., Zhang, D., Dabeer, O.: Spot-the-difference self-supervised pre-training for anomaly detection and segmentation. In: European Conference on Computer Vision, pp. 392–408 (2022). Springer
- [16] Bergmann, P., Jin, X., Sattlegger, D., Steger, C.: The mvtec 3d-ad dataset for unsupervised 3d anomaly detection and localization. *arXiv preprint arXiv:2112.09045* (2021)
- [17] Diers, J., Pigorsch, C.: A survey of methods for automated quality control based on images. *International Journal of Computer Vision* **131**(10), 2553–2581 (2023)
- [18] Tao, X., Gong, X., Zhang, X., Yan, S., Adak, C.: Deep learning for unsupervised anomaly localization in industrial images: A survey. *IEEE Transactions on Instrumentation and Measurement* **71**, 1–21 (2022)
- [19] Cui, Y., Liu, Z., Lian, S.: A survey on unsupervised anomaly detection algorithms for industrial images. *IEEE Access* (2023)
- [20] Liu, J., Xie, G., Wang, J., Li, S., Wang, C., Zheng, F., Jin, Y.: Deep industrial image anomaly detection: A survey. *Machine Intelligence Research* **21**(1), 104–135 (2024)
- [21] Zavrtanik, V., Kristan, M., Skočaj, D.: Draem-a discriminatively trained reconstruction embedding for surface anomaly detection. In: Proceedings of the IEEE/CVF International Conference on Computer Vision, pp. 8330–8339 (2021)
- [22] Dehaene, D., Eline, P.: Anomaly localization by modeling perceptual features. *arXiv preprint arXiv:2008.05369* (2020)
- [23] Liang, Y., Zhang, J., Zhao, S., Wu, R., Liu, Y., Pan, S.: Omni-frequency channel-selection representations for unsupervised anomaly detection. *IEEE Transactions on Image Processing* (2023)
- [24] You, Z., Cui, L., Shen, Y., Yang, K., Lu, X., Zheng, Y., Le, X.: A unified model

for multi-class anomaly detection. *Advances in Neural Information Processing Systems* **35**, 4571–4584 (2022)

- [25] Wyatt, J., Leach, A., Schmon, S.M., Willcocks, C.G.: Anoddpm: Anomaly detection with denoising diffusion probabilistic models using simplex noise. In: *Proceedings of the IEEE/CVF Conference on Computer Vision and Pattern Recognition*, pp. 650–656 (2022)
- [26] Yan, X., Zhang, H., Xu, X., Hu, X., Heng, P.-A.: Learning semantic context from normal samples for unsupervised anomaly detection. In: *Proceedings of the AAAI Conference on Artificial Intelligence*, vol. 35, pp. 3110–3118 (2021)
- [27] Bergmann, P., Fauser, M., Sattlegger, D., Steger, C.: Uninformed students: Student-teacher anomaly detection with discriminative latent embeddings. In: *Proceedings of the IEEE/CVF Conference on Computer Vision and Pattern Recognition*, pp. 4183–4192 (2020)
- [28] Salehi, M., Sadjadi, N., Baselizadeh, S., Rohban, M.H., Rabiee, H.R.: Multiresolution knowledge distillation for anomaly detection. In: *Proceedings of the IEEE/CVF Conference on Computer Vision and Pattern Recognition*, pp. 14902–14912 (2021)
- [29] Yi, J., Yoon, S.: Patch svdd: Patch-level svdd for anomaly detection and segmentation. In: *Proceedings of the Asian Conference on Computer Vision* (2020)
- [30] Massoli, F.V., Falchi, F., Kantarci, A., Akti, S., Ekenel, H.K., Amato, G.: Mocca: Multilayer one-class classification for anomaly detection. *IEEE transactions on neural networks and learning systems* **33**(6), 2313–2323 (2021)
- [31] Roth, K., Pemula, L., Zepeda, J., Schölkopf, B., Brox, T., Gehler, P.: Towards total recall in industrial anomaly detection. In: *Proceedings of the IEEE/CVF Conference on Computer Vision and Pattern Recognition*, pp. 14318–14328 (2022)
- [32] Gudovskiy, D., Ishizaka, S., Kozuka, K.: Cflow-ad: Real-time unsupervised anomaly detection with localization via conditional normalizing flows. In: *Proceedings of the IEEE/CVF Winter Conference on Applications of Computer Vision*, pp. 98–107 (2022)
- [33] Jeong, J., Zou, Y., Kim, T., Zhang, D., Ravichandran, A., Dabeer, O.: Winclip: Zero-/few-shot anomaly classification and segmentation. In: *Proceedings of the IEEE/CVF Conference on Computer Vision and Pattern Recognition*, pp. 19606–19616 (2023)
- [34] Huang, C., Guan, H., Jiang, A., Zhang, Y., Spratling, M., Wang, Y.-F.: Registration based few-shot anomaly detection. In: *European Conference on Computer*

Vision, pp. 303–319 (2022). Springer

- [35] Li, C.-L., Sohn, K., Yoon, J., Pfister, T.: Cutpaste: Self-supervised learning for anomaly detection and localization. In: Proceedings of the IEEE/CVF Conference on Computer Vision and Pattern Recognition, pp. 9664–9674 (2021)
- [36] Yang, M., Wu, P., Feng, H.: Memseg: A semi-supervised method for image surface defect detection using differences and commonalities. *Engineering Applications of Artificial Intelligence* **119**, 105835 (2023)
- [37] Jain, S., Seth, G., Paruthi, A., Soni, U., Kumar, G.: Synthetic data augmentation for surface defect detection and classification using deep learning. *Journal of Intelligent Manufacturing*, 1–14 (2022)
- [38] Rudolph, M., Wehrbein, T., Rosenhahn, B., Wandt, B.: Asymmetric student-teacher networks for industrial anomaly detection. In: Proceedings of the IEEE/CVF Winter Conference on Applications of Computer Vision, pp. 2592–2602 (2023)
- [39] Wang, Y., Peng, J., Zhang, J., Yi, R., Wang, Y., Wang, C.: Multimodal industrial anomaly detection via hybrid fusion. In: Proceedings of the IEEE/CVF Conference on Computer Vision and Pattern Recognition, pp. 8032–8041 (2023)
- [40] Cao, Y., Xu, X., Shen, W.: Complementary pseudo multimodal feature for point cloud anomaly detection. arXiv preprint arXiv:2303.13194 (2023)
- [41] Yen-Chen, L., Florence, P., Barron, J.T., Rodriguez, A., Isola, P., Lin, T.-Y.: inferf: Inverting neural radiance fields for pose estimation. In: 2021 IEEE/RSJ International Conference on Intelligent Robots and Systems (IROS), pp. 1323–1330 (2021). IEEE
- [42] Farshian, A., Götz, M., Cavallaro, G., Debus, C., Nießner, M., Benediktsson, J.A., Streit, A.: Deep-learning-based 3-d surface reconstruction—a survey. *Proceedings of the IEEE* (2023)
- [43] Fan, H., Su, H., Guibas, L.J.: A point set generation network for 3d object reconstruction from a single image. In: Proceedings of the IEEE Conference on Computer Vision and Pattern Recognition, pp. 605–613 (2017)
- [44] Achlioptas, P., Diamanti, O., Mitliagkas, I., Guibas, L.: Learning representations and generative models for 3d point clouds. In: International Conference on Machine Learning, pp. 40–49 (2018). PMLR
- [45] Yang, G., Huang, X., Hao, Z., Liu, M.-Y., Belongie, S., Hariharan, B.: Pointflow: 3d point cloud generation with continuous normalizing flows. In: Proceedings of the IEEE/CVF International Conference on Computer Vision, pp. 4541–4550 (2019)

[46] Melas-Kyriazi, L., Rupprecht, C., Vedaldi, A.: Pc2: Projection-conditioned point cloud diffusion for single-image 3d reconstruction. In: Proceedings of the IEEE/CVF Conference on Computer Vision and Pattern Recognition, pp. 12923–12932 (2023)

[47] Ren, S., Hou, J., Chen, X., He, Y., Wang, W.: Geoudf: Surface reconstruction from 3d point clouds via geometry-guided distance representation. In: Proceedings of the IEEE/CVF International Conference on Computer Vision, pp. 14214–14224 (2023)

[48] Lin, C.-H., Kong, C., Lucey, S.: Learning efficient point cloud generation for dense 3d object reconstruction. In: Proceedings of the AAAI Conference on Artificial Intelligence, vol. 32 (2018)

[49] Choy, C.B., Xu, D., Gwak, J., Chen, K., Savarese, S.: 3d-r2n2: A unified approach for single and multi-view 3d object reconstruction. In: Computer Vision–ECCV 2016: 14th European Conference, Amsterdam, The Netherlands, October 11–14, 2016, Proceedings, Part VIII 14, pp. 628–644 (2016). Springer

[50] Brock, A., Lim, T., Ritchie, J.M., Weston, N.: Generative and discriminative voxel modeling with convolutional neural networks. arXiv preprint arXiv:1608.04236 (2016)

[51] Girdhar, R., Fouhey, D.F., Rodriguez, M., Gupta, A.: Learning a predictable and generative vector representation for objects. In: Computer Vision–ECCV 2016: 14th European Conference, Amsterdam, The Netherlands, October 11–14, 2016, Proceedings, Part VI 14, pp. 484–499 (2016). Springer

[52] Dai, A., Ruizhongtai Qi, C., Nießner, M.: Shape completion using 3d-encoder-predictor cnns and shape synthesis. In: Proceedings of the IEEE Conference on Computer Vision and Pattern Recognition, pp. 5868–5877 (2017)

[53] Tatarchenko, M., Dosovitskiy, A., Brox, T.: Octree generating networks: Efficient convolutional architectures for high-resolution 3d outputs. In: Proceedings of the IEEE International Conference on Computer Vision, pp. 2088–2096 (2017)

[54] Häne, C., Tulsiani, S., Malik, J.: Hierarchical surface prediction for 3d object reconstruction. In: 2017 International Conference on 3D Vision (3DV), pp. 412–420 (2017). IEEE

[55] Dai, A., Nießner, M.: Scan2mesh: From unstructured range scans to 3d meshes. In: Proceedings of the IEEE/CVF Conference on Computer Vision and Pattern Recognition, pp. 5574–5583 (2019)

[56] Kanazawa, A., Tulsiani, S., Efros, A.A., Malik, J.: Learning category-specific mesh reconstruction from image collections. In: Proceedings of the European Conference on Computer Vision (ECCV), pp. 371–386 (2018)

- [57] Wen, C., Zhang, Y., Li, Z., Fu, Y.: Pixel2mesh++: Multi-view 3d mesh generation via deformation. In: Proceedings of the IEEE/CVF International Conference on Computer Vision, pp. 1042–1051 (2019)
- [58] Wang, N., Zhang, Y., Li, Z., Fu, Y., Liu, W., Jiang, Y.-G.: Pixel2mesh: Generating 3d mesh models from single rgb images. In: Proceedings of the European Conference on Computer Vision (ECCV), pp. 52–67 (2018)
- [59] Badki, A., Gallo, O., Kautz, J., Sen, P.: Meshlet priors for 3d mesh reconstruction. In: Proceedings of the IEEE/CVF Conference on Computer Vision and Pattern Recognition, pp. 2849–2858 (2020)
- [60] Zhou, K.: Neural surface reconstruction from sparse views using epipolar geometry. arXiv e-prints, 2406 (2024)
- [61] Gallouédec, Q., Cazin, N., Dellandréa, E., Chen, L.: Simulated franka emika panda robot. arXiv preprint arXiv:2106.13687 (2021)
- [62] Carfagni, M., Furferi, R., Governi, L., Santarelli, C., Servi, M., Uccheddu, F., Volpe, Y.: Metrological and critical characterization of the intel d415 stereo depth camera. Sensors **19**(3), 489 (2019)
- [63] Chen, A., Xu, Z., Zhao, F., Zhang, X., Xiang, F., Yu, J., Su, H.: Mvsnerf: Fast generalizable radiance field reconstruction from multi-view stereo. In: Proceedings of the IEEE/CVF International Conference on Computer Vision, pp. 14124–14133 (2021)
- [64] Wang, P., Liu, L., Liu, Y., Theobalt, C., Komura, T., Wang, W.: Neus: Learning neural implicit surfaces by volume rendering for multi-view reconstruction. arXiv preprint arXiv:2106.10689 (2021)
- [65] Kerbl, B., Kopanas, G., Leimkühler, T., Drettakis, G.: 3d gaussian splatting for real-time radiance field rendering. ACM Transactions on Graphics **42**(4), 1–14 (2023)
- [66] Schonberger, J.L., Frahm, J.-M.: Structure-from-motion revisited. In: Proceedings of the IEEE Conference on Computer Vision and Pattern Recognition, pp. 4104–4113 (2016)
- [67] Heinly, J., Schonberger, J.L., Dunn, E., Frahm, J.-M.: Reconstructing the world* in six days*(as captured by the yahoo 100 million image dataset). In: Proceedings of the IEEE Conference on Computer Vision and Pattern Recognition, pp. 3287–3295 (2015)
- [68] Schonberger, J.L., Radenovic, F., Chum, O., Frahm, J.-M.: From single image query to detailed 3d reconstruction. In: Proceedings of the IEEE Conference on Computer Vision and Pattern Recognition, pp. 5126–5134 (2015)

[69] Schönberger, J.L., Zheng, E., Frahm, J.-M., Pollefeys, M.: Pixelwise view selection for unstructured multi-view stereo. In: Computer Vision–ECCV 2016: 14th European Conference, Amsterdam, The Netherlands, October 11–14, 2016, Proceedings, Part III 14, pp. 501–518 (2016). Springer

[70] Zheng, E., Dunn, E., Jojic, V., Frahm, J.-M.: Patchmatch based joint view selection and depthmap estimation. In: Proceedings of the IEEE Conference on Computer Vision and Pattern Recognition, pp. 1510–1517 (2014)

[71] Zhou, K., Hong, L., Chen, C., Xu, H., Ye, C., Hu, Q., Li, Z.: Devnet: Self-supervised monocular depth learning via density volume construction. In: European Conference on Computer Vision, pp. 125–142 (2022). Springer

[72] Wang, Q., Wang, Z., Genova, K., Srinivasan, P.P., Zhou, H., Barron, J.T., Martin-Brualla, R., Snavely, N., Funkhouser, T.: Ibrnet: Learning multi-view image-based rendering. In: Proceedings of the IEEE/CVF Conference on Computer Vision and Pattern Recognition, pp. 4690–4699 (2021)

[73] Yu, A., Ye, V., Tancik, M., Kanazawa, A.: pixelnerf: Neural radiance fields from one or few images. In: Proceedings of the IEEE/CVF Conference on Computer Vision and Pattern Recognition, pp. 4578–4587 (2021)

[74] Yu, J., Zheng, Y., Wang, X., Li, W., Wu, Y., Zhao, R., Wu, L.: Fastflow: Unsupervised anomaly detection and localization via 2d normalizing flows. arXiv preprint arXiv:2111.07677 (2021)

[75] Wang, G., Han, S., Ding, E., Huang, D.: Student-teacher feature pyramid matching for anomaly detection. arXiv preprint arXiv:2103.04257 (2021)

[76] Lee, S., Lee, S., Song, B.C.: Cfa: Coupled-hypersphere-based feature adaptation for target-oriented anomaly localization. IEEE Access **10**, 78446–78454 (2022)

[77] Yamada, S., Hotta, K.: Reconstruction student with attention for student-teacher pyramid matching. arXiv preprint arXiv:2111.15376 (2021)

[78] Cao, Y., Xu, X., Liu, Z., Shen, W.: Collaborative discrepancy optimization for reliable image anomaly localization. IEEE Transactions on Industrial Informatics (2023)

[79] Horwitz, E., Hoshen, Y.: Back to the feature: classical 3d features are (almost) all you need for 3d anomaly detection. In: Proceedings of the IEEE/CVF Conference on Computer Vision and Pattern Recognition, pp. 2967–2976 (2023)